Chapter 2
Concept and State-of-the-Art

2.1 Purification Concept

Purification of peptide arrays with a density of up to 10,000 different array members per cm^2 requires a concept compatible with the given array format: Synthesis artefacts must be removed in situ, i.e. without the loss of spatial information provided by the synthesis. In addition, the peptides have to be purified simultaneously because external purification of each array member would diminish the benefits gained from combinatorial synthesis and is not feasible for highly resolved arrays. Hence, a concept consisting of three basic elements has been developed: (1) The peptide arrays are synthesized as usual, but a cleavable linker is inserted between surface coating and peptide; (2) After the synthesis, only the full length peptides are elongated with an additional "key" sequence; (3) The entire peptide array is cleaved and transferred to a second solid support, brought into direct contact with the synthesis support. Only full-length peptides rebind via their "key" sequence which has been designed specifically to bind to the surface of the new solid support. This transfer step must be achieved in the highest possible resolution and, most importantly, without mixing of individual spots, i.e. without lateral diffusion (Fig. 2.1).

In the following paragraph, state-of-the-art technologies for the preparation of synthesis surfaces are described. Furthermore, a brief introduction is given to peptide linker chemistry and surface sensitive analysis techniques applied in this work.

2.2 Synthesis Surfaces

Similar to SPPS using modified polymeric beads, peptide array synthesis on a "two-dimensional" surface requires functional groups. These functional groups must be firmly anchored to the support to preserve spatial resolution of the array throughout the entire synthesis process. Furthermore, the surface coating must be inert to a variety of different substances including harsh reagents such as organic

C. Schirwitz, *Purification of Peptides in High-Complexity Arrays*,
Springer Theses, DOI: 10.1007/978-3-319-00807-3_2,

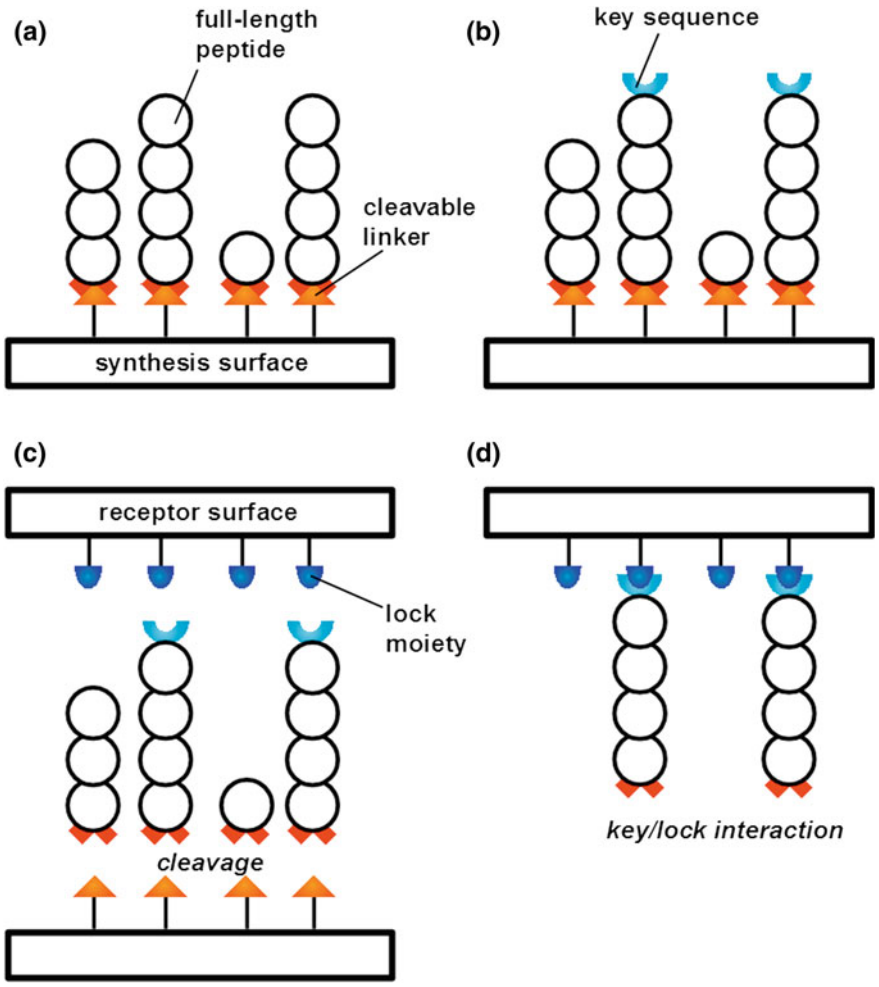

Fig. 2.1 Concept for peptide array purification: **a** The peptide array is synthesized on a surface which bears a cleavable linker. **b** Only full-length peptides obtain an exclusive key sequence in the last synthesis cycle. **c** The synthesis surface is brought into direct contact with a receptor surface while the cleavage is conducted. Peptides and fragments are released. **d** Only full-length peptides rebind to the receptor surface due to a specific "lock" molecule immobilized on the receptor side. Fragments are removed by washing

acids and bases. Standard microscopy slide glass (SiO_2) is used for the micro particle-based peptide array synthesis in the laser printer approach [1]. In contrast, the CMOS micro chips are equipped with aluminum electrodes (Al/Al_2O_3, "Peptide Chip 5") [2, 3]. Both types of surfaces are routinely coated with polymers on the basis of methacrylates whose side-chains can be functionalized with amino groups. For surface sensitive studies, we additionally use silicon wafers which are similarly treated. The following chapter provides an overview of

existing surface preparation techniques that have been applied and, in part, enhanced in this work.

2.2.1 Cleaning and Activation

Prior to surface functionalization, the surface has to be thoroughly cleaned in order to remove any organic or inorganic contamination. In addition, the upper passivating oxide layers must be "activated" to render them reactive. In this work, glass slides (SiO_2), micro chips (Al/Al_2O_3), and silicon wafers, slices of a silicon single crystal (100) with a thin silicon oxide layer, are applied as substrates for peptide synthesis. Driven by the progress in semiconductor research, cleaning techniques for silicon wafers have been investigated and enhanced since the early 1950s [4]. In general, wet chemical cleaning using hydrogen peroxide solutions is wide spread. In our group, the common cleaning and activation process for SiO_2 surfaces (silicon wafers and glass slides) is based on treatment in hot piranha solution, a mixture of 30 % (v/v) H_2O_2 (30 % (v/v) aqueous solution) and 70 % (v/v) concentrated H_2SO_4 [5]. However, hot piranha solution is corrosive to metals and, therefore, inadequate to pretreat susceptible micro chips [6]. Instead, the micro chip surfaces are cleaned and activated by UV irradiation in air according to approved protocols [7]. In general, treatment with piranha solution or UV irradiation generates defined oxide layers bearing reactive hydroxy groups on SiO_2 or Al_2O_3 surfaces [6, 8]. Alkylchlorosilanes, alkylalkoxysilanes, and alkylaminosilanes are known to covalently bind to such "activated" surfaces forming self assembled monolayers (SAMs) [9, 10]. Hence, SAMs of organosilanes represent highly stable anchor groups for functional surface coatings as discussed in the following paragraph.

2.2.2 Surface-Initiated ATRP

The first surface coatings in the micro particle-based peptide array synthesis were films of poly(ethylene glycol) methacrylate (PEGMA) which were prepared by deposition of an olefin silane SAM, subsequent ozonization of the olefin, and radical graft polymerization with PEGMA ($M_n = 360$ g/mol, *Sigma-Aldrich*, Steinheim/Germany) [5]. PEGMA is a commercial macromonomer with an average side-chain length, in this case, of 4 to 5 ethylene glycol (EG) units. In the course of a polymerization only the methacrylate backbone is polymerized whereas the side-chains remain unaffected. PEGMA films are characterized by a high density of functional groups (up to 40 nmol/cm^2 on a 100 nm thick film), intrinsic protein repelling properties, and good stability to chemical treatments as present in peptide synthesis [5]. The preparation of PEGMA films has been facilitated using the surface-initiated atom transfer radical polmyerization (siATRP) technique developed by HUANG and WIRTH in 1997 [11]. Since this

development, siATRP has become a standard technique for graft polymer coatings [12, 13]. By means of siATRP even our susceptible micro chip surfaces can be coated with PEGMA films in full control of the resulting film thicknesses [7]. First, the surface is activated with piranha solution or by UV irradiation. Then, it is silanized with a SAM of 2-bromo-*N*-(3-triethoxysilyl propyl) isobutyramide (bromine silane (**1**), Fig. 2.2). The tertiary bromine of the silane is the starting point of a controlled radical polymerization, also referred to as *living polymerization,* which can be conducted with various transition metal catalysts/ligand systems [14, 15]. The advantages of the ATRP technique include fast rates of polymerization, narrow molecular weight distributions, high monomer conversion, and precise control of the polymer composition [16].

In our group, the catalyst is typically a Cu^{I} salt with additional organic ligands such as 2,2′-bipyridine (bpy) or 1,1,4,7,7-pentamethyldiethylenetriamine (PMDETA) as first described by WANG and MATYJASZEWSKI in 1995 [17]. Further optimization of the brush polymer composition to meet the requirements of biological assays with peptide arrays led to the development of PEGMA-co-PMMA films [18]. These films consist of different mole fractions of PEGMA and polymethylmethacrylate (PMMA) which can be controlled via the monomer concentration in the polymerization solution. PEGMA and methylmethacrylate (MMA) are statistically inserted into the growing polymer chain. The more MMA used the fewer PEG side-chains appear in the film. This reduces the number of functional groups available for peptide synthesis (see Fig. 2.2), but on the other hand, provides better accessibility for proteins such as antibodies or enzymes [18]. If the hydrophilic PEG moieties are reduced, a higher contact angle and, thus, a more hydrophobic character of the surface is observed. However, nonspecific protein adsorption is efficiently suppressed even with a low mole fraction of PEGMA. In this work, a graft copolymer composition of 10 % (n/n) PEGMA and 90 % (n/n) PMMA (10:90-PEGMA-co-PMMA) was the standard surface coating for the peptide array synthesis because it has proven to be the best compromise between intrinsic protein repelling properties and compatibility to standard biological applications (i.e. reference immunostainings, see 5.3.10). Independent of the copolymer composition, the PEG-OH side-chains are further modified with Fmoc-β-alanine to yield amino groups necessary for the peptide synthesis (see Fig. 2.2) [5, 7, 18].

2.2.3 Cleavable Linkers

Along with solid phase chemistry, numerous cleavable linkers, which facilitate the release of compounds from the solid support after the peptide synthesis, have been developed [19, 20]. During the synthesis, the linker determines the allowable chemistry because it has to fit into the protecting group strategy (see 1.1.3 and 1.1.4) and must not release compounds before the synthesis has been completed. Furthermore, the choice of the linker also depends on the type of compound synthesized: The cleaving conditions may not compromise the integrity of the

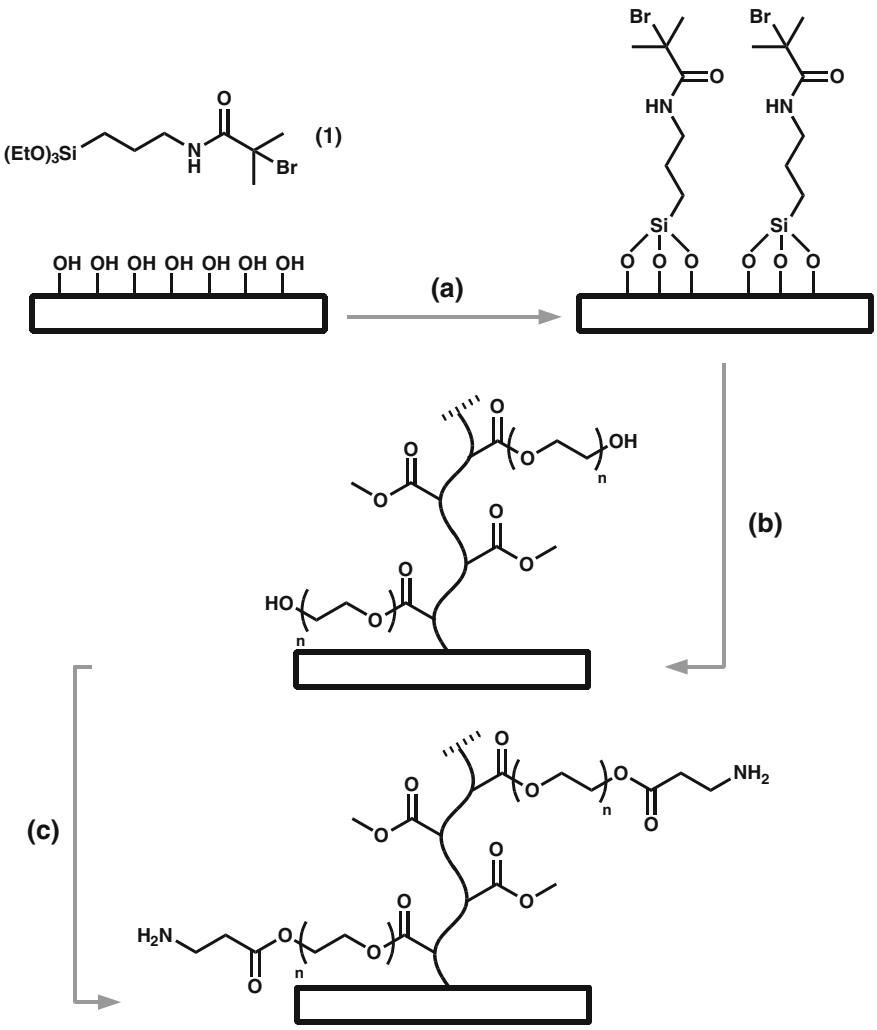

Fig. 2.2 Silanization and siATRP: **a** An activated surface bearing hydroxyl groups is silanized with bromine silane (**1**); **b** The resulting silane SAM acts as an anchor group and surface-bound initiator for the siATRP with MMA and PEGMA. The polymethacrylate backbone polymerized in the siATRP is only depicted schematically. **c** Hydroxyl groups in the side-chain of PEGMA can be esterified with β-alanine to yield amino groups

product or the yield. In MERRIFIELD's first approach peptides were cleaved from the resin by saponification or, in case of halogenated resins, by acid halide treatment [21]. In this initial approach, the linker can be considered part of the solid support, because the peptide is directly anchored to the resin by an ester bond. However, such *integral* linkers are disadvantageous in several respects: Exact control of the loading is difficult, comparatively harsh chemical conditions are needed to cleave

the product (e.g. HF), and steric and electronic properties of the resin can affect the cleavage reaction [19]. Thus, numerous linkers which allow for post-modification of the resin and for "mild" cleavage conditions are the current ideal. Established acid-labile compounds in SPPS are, for example, the WANG linker [22], the SASRIN (super acid sensitive resin) linker, [23, 24] the PAL (peptide amide linker) [25, 26], and the RINK type linkers [27] (Fig. 2.3a–d). Besides acid-labile linkers, many other linkers exist which can, for instance, be released by electrophilic, nucleophilic, oxidative, reductive, photo-induced, or metal-assisted cleavage [19, 20]. However, in the N^{α}-Fmoc strategy, weak acid-labile linkers are advantageous: They allow for side-chain deprotection and peptide cleavage in a single step and, thus, do not jeopardize peptide integrity. In general, slight modifications of the linker structure can have a strong impact on the cleavage efficiency and stability which is why many variations of the described linkers exist [19].

Besides acid-labile linkers, another important group is the "safety-catch" linkers. In general, safety-catch linkers are sensitive to nucleophiles, but cleavage requires at least two successive steps. First, the linker is destabilized. Then, the peptide can be released by nucleophilic attack under very mild conditions. Examples of safety-catch linkers are the carboxy FRANK linker (2-(1-*tert*butyloxycarbonyl-4-methyl-imidazol-5-yl)-2-hydroxy aceticacid dicyclohexylamine, Fig. 2.3f) which can be destabilized by TFA treatment and cleaved in aqueous buffer, [28, 29] or aryl hydrazine linkers (WIELAND linkers) such as Fmoc-hydrazinobenzoicacid (Fmoc-HBA, Fig. 2.3e), which can be cleaved by mild oxidation of the hydrazine bond and subsequent attack of a nucleophile [30, 31]. The choice of nucleophile determines the functional group formed at the C-terminal end of the peptides. For example, cleavage in (alkaline) aqueous solutions yields carboxylic acids whereas cleavage with amines yields amides. The ability to achieve desired functional groups at the C-terminus through prudent choice of nucleophile, allows for precise control over the functionality of the resulting peptide.

2.3 Introduction to Surface Analytical Techniques

2.3.1 UV/Vis Photospectrometry

In each coupling cycle of the N^{α}-Fmoc strategy of SPPS the N-terminal Fmoc protecting group is cleaved prior to attachment of the next amino acid in the sequence (see 1.1.3). An intermediate in the cleavage step is the piperidine dibenzofulvene adduct (PDFA) which has an absorption maximum at 301 nm (Fig. 2.4).

The concentration of PDFA in the deprotection solution can be measured using UV/Vis photospectrometry by comparing its absorption to that of a blank solution. Hence, the amino group loading on the surface, i.e. the derivatization grade (DG) cm^2, can be calculated from the concentration of PDFA in the deblocking solution.

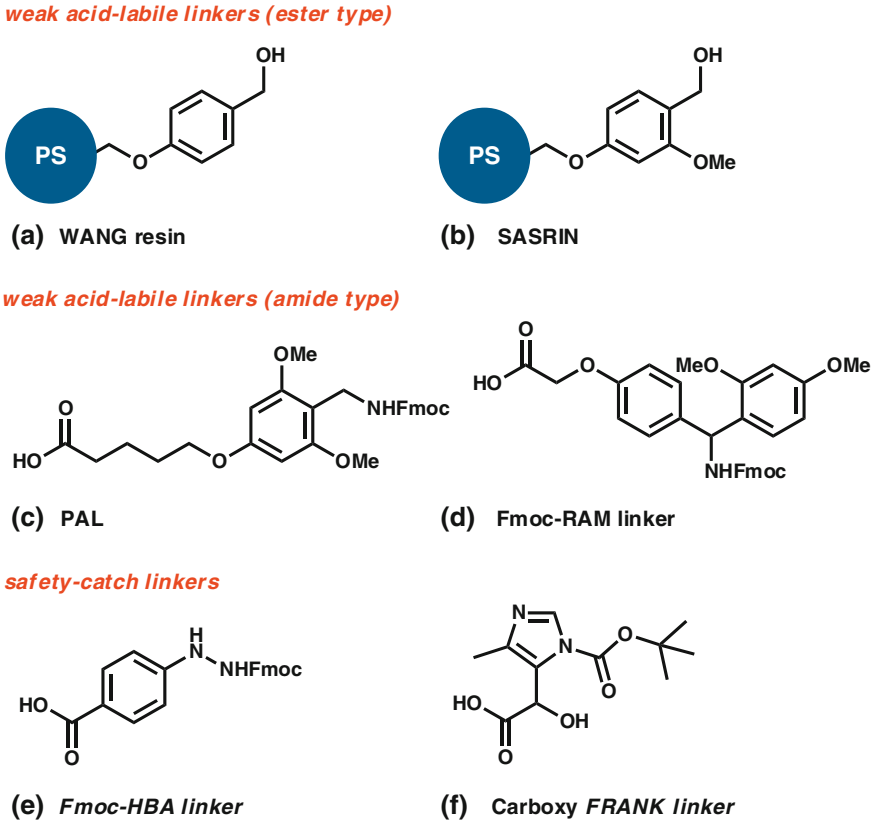

Fig. 2.3 Examples of cleavable linkers in SPPS: **a**, **b** Standard resin-bound linkers that yield free acids upon cleavage. **c**, **d** Amide-type linkers yielding peptide amides. **e**, **f** Safety-catch linkers that can be destabilized and cleaved in aqueous media

According to LAMBERT–BEER's law, the DG of the surface is given by Eq. 2.1 [5, 32]. In our group, a basic calibration of the *SmartSpecs Plus* (*Bio-Rad Laboratories*, Munich/Germany) photospectrometer yielded a molar extincition coefficient of $\varepsilon = 5129$ L·mol^{-1}·cm^{-1} for the deblocking solution, respectively [5, 33]. However, other groups reported different molar extinction coefficients [34] and fluctuating DG values which can most likely be attributed to the equilibrium of PDFA and dibenzofulvene/piperidine [35]. Therefore, this method is not considered to provide absolute quantities, but values which can be compared to results obtained in previous works in the same manner [33, 36].

$$DG = \frac{n}{A} = \frac{E \cdot V}{\varepsilon \cdot d \cdot A} \tag{2.1}$$

Equation 2.1: Derivatization grade (DG) of surfaces calculated upon Fmoc release. n = amount of substance in moles, A = surface area covered with

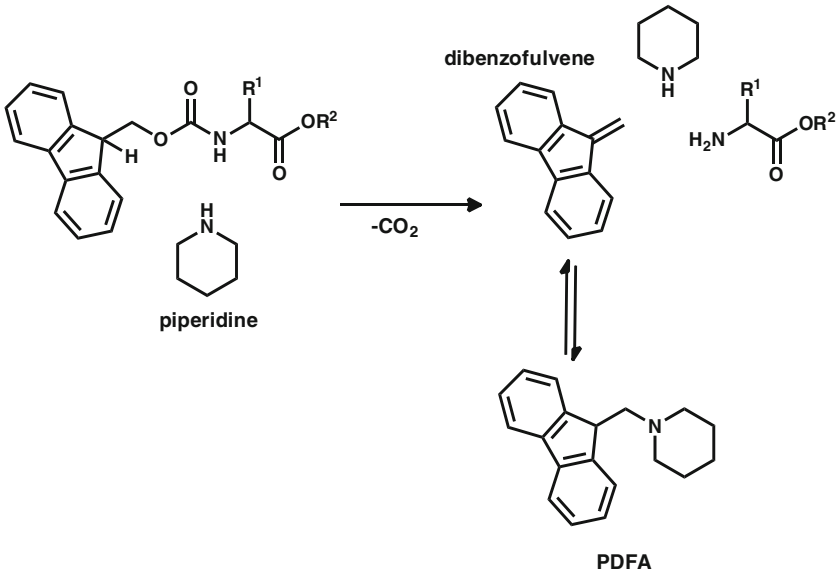

Fig. 2.4 Fmoc cleavage and PDFA formation: Deprotection of an Fmoc-protected amino group with 20 % piperidine in DMF yields dibenzofulvene and the free amino group. In presence of piperidine, dibenzofulvene forms the piperidine dibenzofulvene adduct (PDFA) which has an absorption maximum at 301 nm

deprotection solution, E = extinction, V = applied volume of 20 % (v/v) piperidine in DMF, ε = extinction coefficient, d = path length of cuvette.

To determine the DG of irregularly shaped silicon wafer pieces, the surface area A was calculated from the weight of the wafer piece. For the Si(100) wafers used in this work a conversion factor of 8.185 $cm^2 \cdot g^{-1}$ has been assigned.

2.3.2 Spectroscopic Ellipsometry

In spectroscopic ellipsometry information about film thicknesses, optical constants, surface roughness, and material micro structures in multilayered systems is gained by measuring the polarization state of light [37]. A collimated polarized light beam is reflected from (or transmitted through) the sample surface to a detector which analyzes changes in polarization caused by the material. Two major advantages of ellipsometry are the high sensitivity ranging from layers of single atoms to a few μm-thick films and the nondestructive measuring principle which also works under liquids [37, 38]. For maximum sensitivity, the angle of incidence and the wavelength of the incident beam are controlled. This procedure is referred to as variable angle spectroscopic ellipsometry (VASE).

In general, ellipsometry uses a beam of linearly polarized light whereby the *s*- and *p*-components of the beam are analyzed. *s* refers to the light vector component perpendicular to the plane of incidence and *p* refers to the component parallel to the plane of incidence. The beam is directed to a reflecting surface so that the *s* and *p* components of the electrical field vector $\vec{E}$ are in phase with each other. Due to interaction with the material, the *s*- and *p*-components are phase-shifted. The *s* component is mostly reflected, whereas the *p* component is mostly refracted into the optically denser medium. This causes the projection of the electrical vector to trace out an ellipse in a plane perpendicular to the propagation direction of the beam. The azimuthal angle of the electric field vector along the major axis of the ellipse relative to a plane of reference, the ellipticity, and sometimes the handedness (right- or left-handed) of the electric vector are used to obtain information about the material [37]. Instead of absolute intensities, ellipsometry uses the ratio of reflected and incident light intensity *R* which simplifies the instrumentation. The ratio of reflected and incident intensity is described by the square value of the Fresnel reflection coefficient *r* as shown in Eq. 2.2.

$$\begin{aligned} R_s &= \frac{I_r^s}{I_0^s} = |r_s|^2 \\ R_p &= \frac{I_r^p}{I_0^p} = |r_p|^2 \end{aligned} \tag{2.2}$$

Equation 2.2: Ratio of reflected and incident light intensity *R*. I = intensity, r = Fresnel reflection coefficient (indices: r = reflected, 0 = incident, s = s-polarized, p = *p*-polarized).

Furthermore, the Fresnel reflection coefficient is linked to the components of the electric vector *E* and the refractive indices η as shown in Eq. 2.3 (Fig. 2.5).

$$\begin{aligned} r_s &= \frac{E_r^s}{E_0^s} = \frac{\eta_1 \cos(\vartheta_1) - \eta_2 \cos(\vartheta_2)}{\eta_1 \cos(\vartheta_1) + \eta_2 \cos(\vartheta_2)} \\ r_p &= \frac{E_r^p}{E_0^p} = \frac{\eta_2 \cos(\vartheta_1) - \eta_1 \cos(\vartheta_2)}{\eta_2 \cos(\vartheta_1) + \eta_1 \cos(\vartheta_2)} \end{aligned} \tag{2.3}$$

Equation 2.3: Fresnel reflection coefficients. r = Fresnel reflection coefficient, E = component of the electric field vector, η = refractive index, ϑ = incident

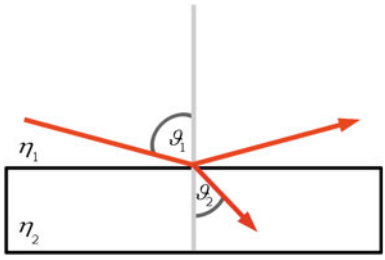

Fig. 2.5 Reflection and refraction of a beam of light at the interphase between two media

angle (indices: r = reflected, 0 = incident, s = s-polarized, p = p-polarized, 1 = medium A, 2 = medium B).

According to the Snell law the ratio of the sines of the incident angles is equivalent to the opposite ratio of the refractive indices (see Eq. 2.4).

$$\frac{\sin(\vartheta_1)}{\sin(\vartheta_2)} = \frac{\eta_2}{\eta_1} \tag{2.4}$$

Equation 2.4: SNELL law of refraction. The ratio of the sines of the incident angles is equivalent to the opposite ratio of the refractive indices.

In the fundamental equation of ellipsometry, the Fresnel coefficients are related to the amplitude factor, Ψ, and the phase factor, Δ (see Eq. 2.5). Measurements of Ψ and Δ are directly related to the material properties and can also be used to calculate the thickness of individual layers in multilayered systems.

$$\frac{r_p}{r_s} = \tan\Psi \cdot e^{i\Delta} \tag{2.5}$$

Equation 2.5: Fundamental equation of ellipsometry. Ψ = amplitude factor, i = imaginary unit, Δ = phase factor.

2.3.2.1 Ellipsometry in Multilayered Systems

In real systems, multilayers and additional parameters such as surface roughness make an algebraic solution complicated. In multilayered systems, the reflected light is a superposition of all beams reflected from the different interphases (see Fig. 2.6). Therefore, a regression analysis is required to identify unknown parameters such as film thickness or optical constants.

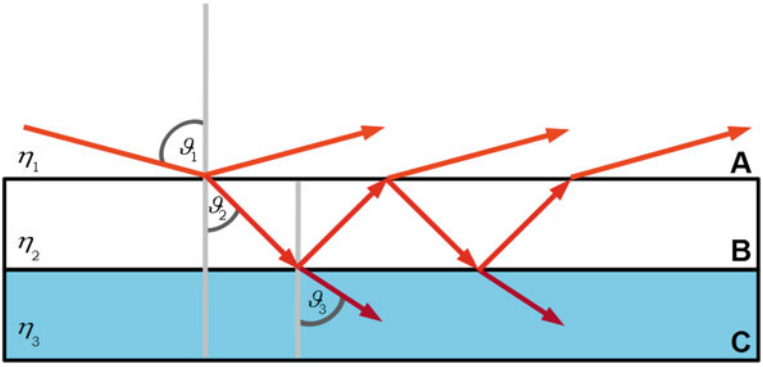

Fig. 2.6 Reflection and refraction in a three layer system: The incident beam is reflected and refracted at the interphase between medium A and B. The refracted beam in medium B is again reflected and refracted at the interphase between medium B and C

In the present work, ellipsometry has been employed to determine the thickness of organic layers on solid supports. The FRESNEL coefficients for such three layer systems as depicted in Fig. 2.6 (medium A = air, medium B = organic layer, medium C = support) are given by Eq. 2.6.

$$r_s = \frac{r_s^{12} + r_s^{23} \cdot e^{-i2\varphi}}{1 + r_s^{12} + r_s^{23} \cdot e^{-i2\varphi}}$$
$$\text{with } \varphi = 2\pi\left(\frac{d}{\lambda}\right)\eta_2\cos(\vartheta_2) \tag{2.6}$$
$$r_p = \frac{r_p^{12} + r_p^{23} \cdot e^{-i2\varphi}}{1 + r_p^{12} + r_p^{23} \cdot e^{-i2\varphi}}$$

Equation 2.6: FRESNEL reflection coefficients for a three layer system. d = thickness of layer B with the refractive index η_2, λ = wavelength (indices: *1* = medium A, *2* = medium B, *3* = medium C).

According to Eq. 2.6 the thickness of medium B can be obtained by the phase shift of a wave which is reflected at the interphase of medium B and medium C compared to a wave which is reflected at the interphase of medium A and medium B.

To determine the film thicknesses of organic layers on a reflecting substrate, another parameter required is the refractive index of the organic layer. If the refractive indices of these materials are unknown, the CAUCHY model can be applied to parametrize the values (see Eq. 2.7) [39]. According to the CAUCHY model the refractive index of the material decreases with the square of the wavelength which is a good approximation as long as the material does not absorb light at the respective wavelength. To increase the accuracy, measurements are usually performed at multiple wavelengths.

$$\eta(\lambda) = \eta_0 + \frac{Y}{\lambda^2} \tag{2.7}$$

Equation 2.7: CAUCHY parametrization of the refractive index. Y = CAUCHY parameter.

For further information on the principles of ellipsometry, the setup of an ellipsometer, and applications thereof reference is made to the literature [37, 40].

2.3.3 Scanning Electron Microscopy

Scanning Electron Microscopy (SEM) uses a beam of electrons to raster over a surface. Compared to light microscopy, the use of electrons with energies of typically 1–40 keV enhances the maximum achievable resolution. According to the DE BROGLIE relation, the wavelength of such high energy electrons is smaller than the length of atomic bonds, which, in theory, should be sufficient to display

atoms. However, the electron beam has to be focused by a setup of electromagnetic fields which limits the maximum resolution [37]. Hence, the instrument provides the user with a 10x–300,000x magnified image of the target and can display structures and topographies in the nm range which is about 100 fold higher than visible light microscopy [41].

SEM uses interaction of the incoming electrons with surface atoms for imaging: Penetration of the electron beam results in an emission of photons or electrons from the sample which are collected and analyzed in different detectors. SEM works at reasonable costs and is a preferred starting tool for materials characterization.

There are mainly three types of images produced in an SEM: *Primary electron* images, *secondary electron* images, and *elemental X-ray maps*. In general, an electron entering a sample can undergo inelastic scattering with atomic electrons or elastic scattering with atomic nuclei of the material. High-energy electrons reaching the detector are referred to as *primary electrons*. In principle, they have been scattered elastically at the atomic nuclei of the sample without loss of kinetic energy. Therefore, a *primary electron* is also called *backscattered electron* (BSE). However, inelastic scattering with atomic electrons and, thus, a loss of energy can occur before an electron has travelled from source to detector. *Secondary electrons* (SEs) are generated when a *primary electron* hits an electron in the material and transfers enough energy to eject it. Since energy is needed to overcome the binding energy of the electron in the material *secondary electrons* are detected at lower energies than BSEs. In SEM, electrons with energies of less than 50 eV, by convention, are referred to as *secondary electrons* (SE). Most of the SEs are emitted from the first few nm of the surface. Since there are three possible ways of SE emission, the group is further divided: SEIs are generated when the beam enters the sample, SEIIs are emitted when a BSE leaves the sample, and SEIIIs are produced by BSEs interacting with materials in the analysis chamber which are not related to the sample. The SE mode is the standard mode in SEM because it provides the best topographic information. The number of SEs produced changes with the slope of the surface, whereas the change in emission volume is comparatively small.

The third group of interactions is (X-ray) photon emission: When the primary electron collides with a core electron in the solid and ejects it, an electron coming from an outer shell falls back to fill the gap. The resultant excess of energy can either be emitted as a characteristic photon or excite a valence-shell electron to leave the atom. The latter is called an AUGER electron and is detected in the group of SEs. Photons emitted from surface atoms usually have energies in the X-ray region. Since the energy of the photon is characteristic of the element from which it is emitted, sorting the photons by energy provides valuable information on surface composition. X-ray emission in a SEM is not used for direct imaging but for an elemental map of the surface similar to XPS (see 1.3.4). The spatial resolution of such X-ray maps in SEM is, however, limited to approximately 500 nm because the primary electrons can travel through a certain volume of the material and cause interactions at many positions [37].

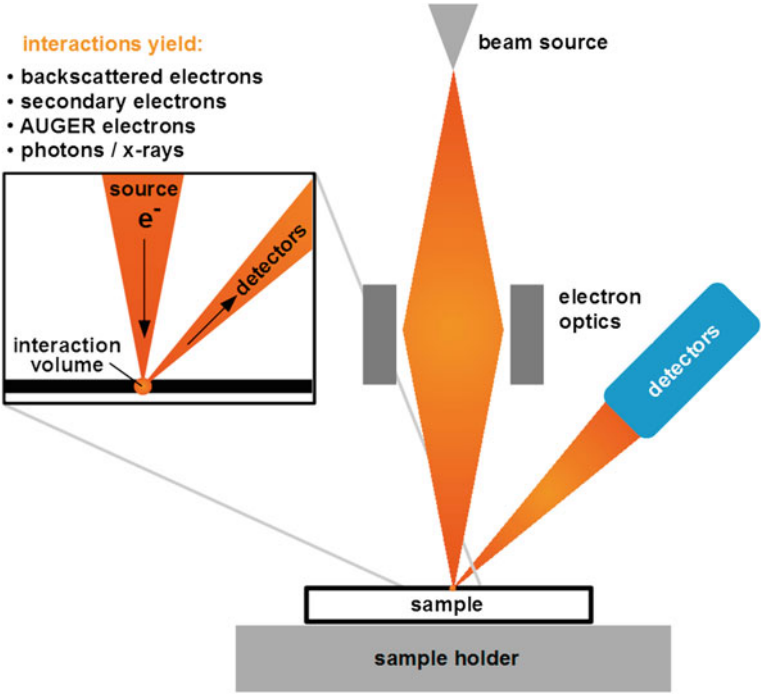

Fig. 2.7 Schematic of an SEM setup: A beam generated by an electron source is focused with electron optics and rastered over a sample. The incident beam causes different interactions with the surface atoms which are detected and used for imaging (primary and secondary electrons, Auger electrons) or elemental mapping (X-rays)

The setup of an SEM is arranged in a high vacuum chamber and comprises an electron source, electron optics, a movable sample-holder, as well as several detectors (Fig. 2.7). The electron source can either be a thermionic (W or LaB_6) or a field emission gun. Although the use of the SEM requires vacuum-compatible samples, operation of the microscope is actually very easy. Insulating samples can be studied with low primary beam voltages (<2 keV) or coated with a thin film of carbon, gold, or some other metal to avoid charge build-up [37].

For further information on imaging modes, detectors, electron optics, sample preparation, and applications, reference is made to the literature [37, 41, 42]

2.3.4 X-ray Photoelectron Spectroscopy

X-ray photoelectron spectroscopy (XPS) is a surface sensitive analysis technique which provides information on the chemical composition of matter. Based on the discovery and explanation of the photoelectric effect by HERTZ and EINSTEIN, [43, 44]

as well as the pioneering work of SIEGBAHN and co-workers [45, 46] modern spectrometers are widely used in materials analysis. Besides AUGER electron spectroscopy (AES) and secondary ion mass spectrometry (SIMS), XPS is the one of the most dominant surface analysis techniques [37]. In contrast to ultra-violet photoelectron spectroscopy (UPS), which provides information on the character of molecular orbitals, XPS is capable of identifying atoms and their concentration in a defined analysis volume. The technique, which is also referred to as *electron spectroscopy for chemical analysis* (ESCA), uses high energy photons in the form of monochromatic X-rays to ionize surface atoms. The kinetic energy, E_{kin}, of ejected electrons is measured by a detector. Given the energy of the X-ray photon the binding energy (E_b) of the electron can be calculated by Eq. 2.8.

$$E_b = h \cdot v - E_{kin} \tag{2.8}$$

Equation 2.8: Binding energy of electrons detected in XPS. E_b = binding energy, v = frequency, h = PLANCK'S constant, E_{kin} = kinetic energy.

The binding energy is characteristic of the orbital and atom the electron it is ejected from and, thus, allows for a detailed analysis of the surface composition. In general, E_b varies with the effective nuclear charge an electron "experiences" in a multi-electron atom.

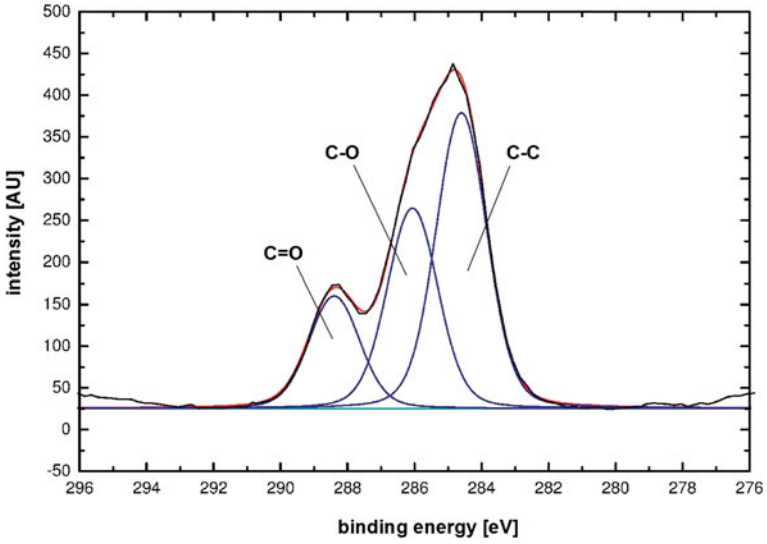

Fig. 2.8 Chemical shift of the C1s peak in XPS: The carboxy C1s signal of a PEGMA-co-PMMA film on a Si(100) wafer is shifted to higher binding energy (288.39 eV), followed by the ether C1s signal of carbon with a single-bonded oxygen (286.06 eV). The alkylic C1s signal was normalized to 284.60 eV

2.3.4.1 Signals and Shifts

In XPS, the energy of the photons is sufficient to eject electrons from core levels, whereas in UPS only electrons from valence levels can be ejected. Hence, XPS provides information which is almost independent of the chemical species the atom is part of. However, due to changes in the effective nuclear charge with different chemical environments electron peaks from the same orbital can show *chemical shifts*: The higher the effective nuclear charge the higher is the binding energy of an electron. Since the effective nuclear charge of an atom depends on the electronegativity of the binding partner, higher binding energies are detected in the presence of a more electronegative binding partner and *vice versa*. Figure 2.8 shows the C1s area of a PEGMA-co-PMMA film (see 1.2.2) polymerized on a Si(100) wafer. The carboxy (C=O) C1s signal is shifted to higher binding energy (288.39 eV), followed by the ether (C–O) C1s signal at 286.06 eV. The alkylic (C–C) C1s signal was normalized to a binding energy of 284.60 eV. Even higher shifts than observed for different chemical environments can be caused by different oxidation states of an atom [37]. Chemical shifts are analytically useful because they provide more detailed information on the chemical state of atoms.

Another analytically useful effect in XPS is spin-orbital splitting. For example, the different energy levels of p-orbitals with $j = 1/2$ or $j = 2/3$ (j = total angular momentum) result in doublet peaks. The spin-orbital splitting is predictable and can help to identify unknown lines in a spectrum. Spin-orbital splitting increases with the nuclear charge ($\sim Z^4$) and is, thus, more prominent for heavy atoms. In addition, spin-orbital splitting also spin–spin splitting can occur when paramagnetic materials are studied.

Furthermore, a spectrum often shows *satellite peaks* which are caused by interaction of electrons. In case an ejected electron hits an electron in a valence level and transfers energy on this second electron, it can either eject the second electron (*shake-off* electron) or excite it to an unoccupied higher level (*shake-up* electron). In both cases the photoelectron loses part of its kinetic energy and appears at higher binding energy. The probability of such interactions is low which causes a low intensity of satellite peaks. However, together with the chemical shift interaction with valence electrons can help to identify chemical states [37]. In addition, AUGER electron peaks (see 2.3.3) can appear in the XP spectrum. In many cases they show larger chemical shifts than core-level peaks and, thus, help to identify unknown spectral lines. An additional benefit of AUGER electrons is that their energy is independent of the photoelectron energy. In AES no monochromatic X-rays are required.

2.3.4.2 Spectrometer

An X-ray photoelectron spectrometer typically consist of an ultra-high vacuum chamber ($p < 10^{-7}$ mbar), an X-ray source (typically an Al- or Mg-coated anode which is bombarded with electrons from a high-voltage cathode), an X-ray

monochromator, a movable sample holder, and a detector setup (e.g. a hemispherical sector). Mg K_α (1256.6 eV) or Al K_α (1486.6 eV) radiation is directed to the sample at a controlled angle of incidence. The informational depth in the case of polymers is typically in the range of 7 nm and reaches a maximum of 10 nm [47]. The spot size of newer instruments can be as small as 3 μm in diameter (or 30 nm if X-rays from a synchrotron are used) [47], but is usually in the mm-range. If a high lateral resolution is required, techniques such as AES and SIMS can alternatively be applied. Furthermore, small-spot analysis for high lateral resolution lowers the count rate of photoelectrons and must be compensated by longer spectrum acquisition times [47]. However, XPS has the advantage of a more developed chemical state analysis and fewer problems in terms of induced sample damage [37].

To avoid charge build-up and related signal shifts, the sample holder in XPS is grounded. The FERMI levels of the sample and the spectrometer are equal. As a consequence, a contact potential exists between the sample and the spectrometer because the work function, Φ_{sp}, of the spectrometer is higher than the work function of the sample. Hence, the work function of the spectrometer has to be considered in the calculation of the binding energy, as shown in Eq. 2.9, because the photoelectron needs a small additional amount of energy to transfer to vacuum level [47]. In general, the FERMI level of the spectrometer serves as an internal reference for the calculation of binding energies.

$$E_b = h \cdot \nu - \Phi_{sp} - E_{kin} \tag{2.9}$$

Equation 2.9: Binding energy in XPS taking into account the work function of the spectrometer Φ_{sp}.

2.3.4.3 Quantitative Analysis

A major benefit of XPS is that quantitative information on the sample composition, i.e. relative atomic concentrations, can be gained. Integration of the signals in ESCA after appropriate background subtraction provides values which correspond to the fraction of respective atoms in the analysis volume. Background noise arises from X-ray scattering and further interaction of ejected photoelectrons in the material. In principle, the uncertainty of quantitative measurements can vary up to 30 %, but individual calibration of the instrument and relative measurements, e.g. reference measurements of an internal or external standard, greatly improve the accuracy [37].

The intensity of photoelectron peaks depends on several parameters which must be considered in a quantitative comparison of ESCA features. The exact term for the intensity, I_A, of a core-level electron, A, in XPS is shown in Eq. 2.10 [48].

$$I_A = \sigma_A(hv)\, D(E_b) \int_x^y \int_{\gamma=0}^{\pi} \int_{\phi=0}^{2\pi} L_A(\gamma) \int_x^y \int_{\gamma=-\infty}^{\infty} \int_x^y \int_{x=-\infty}^{\infty} J_0(xy) T(wy\gamma\phi E_b)$$

$$\int_x^y \int_{z=0}^{\infty} N_A(xyz)\, e^{\frac{-z}{\lambda_A(E_b)\cos\theta}}\, dxdydzd\phi d\gamma \tag{2.10}$$

Equation 2.10: Term for absolute signal intensity of a core-level electron A in XPS. $\sigma_A(hv)$ = photoionization cross-section, $D(E_b)$ = detection efficiency of photoelectrons, $L_A(\gamma)$ = angular asymmetry of the photoelectron intensity, J_0 = properties of the X-ray line in the detection plane, T = transmission function of the energy analyzer, N_A = atomic density at position xyz, γ = angle between incident beam and analyzer aperture, ϕ = azimuth angle, $\lambda_A(E_b)$ = attenuation length as a function of binding energy, θ = emission angle of the photoelectron.

Since a numerical solution of this term is difficult a less complex equation for the signal intensity is provided in Eq. 2.11. For a good approximation it can be assumed that device specific parameters such as X-ray line properties or detection efficiency are constant for measurements with the same setup. A transmission function, $T(E_b)$, which describes the detection probability of photoelectrons at different kinetic energies is determined once experimentally and then routinely used to normalize spectra.

$$I_A = \sigma_A N_A \lambda_A(E_b)\, T(E_b)\, \cos\theta \left[1 - e^{\frac{-z}{\lambda_A(E_b)\cos\theta}}\right] \tag{2.11}$$

Equation 2.11: Approximation for the relative signal intensity of a core-level electron A in XPS. $T(E_b)$ = transmission function of the spectrometer.

Hence, for homogeneous samples atomic concentrations in the analysis volume can be determined by intensity ratios according to Eq. 2.12 given that the signals are measured under identical experimental conditions.

$$\frac{I_A}{I_B} = \frac{\sigma_A}{\sigma_B} \frac{N_A}{N_B} \frac{\lambda_A\left(E_b^A\right)}{\lambda_B\left(E_b^B\right)} \; and \; \frac{N_B}{N_A} = \frac{\sigma_A}{\sigma_B} \frac{\lambda_A\left(E_b^A\right)}{\lambda_B\left(E_b^B\right)} \frac{I_B}{I_A} \tag{2.12}$$

Equation 2.12: Intensity ratio and atomic concentration of two elements A and B in XPS.

In this approximation the intensity of a photoelectron peak only depends on ionization cross-section σ and the attenuation length, λ, of an electron exiting the sample. Theoretical cross-sections of electrons in their respective orbitals based on calculations have been published by SCOFIELD [49]. Attenuation lengths depend on the kinetic energy of the X-ray photons, the binding energy of the corresponding photoelectron, and the angle of emission. A common way to calculate attenuation lengths in alkylic monolayers is based on a linear fit introduced by BAIN and co-workers [50]. However, for the spectrometer used in this work an exponential fit according to Eq. 2.13 showed better agreement to experimental data and was, thus, applied instead [51].

$$\lambda_A(E_b) = 0.59 \cdot e^{\left(\frac{594.26 - E_b}{150.43}\right)} + 19.39 \tag{2.13}$$

Equation 2.13: Exponential fit for the attenuation length of photoelectrons in alkylic monolayers based on experimental data by STADLER [51].

Cross-sections and attenuation lengths for atomic orbitals referred to in this work are listed in 5.1.4 (Table 6). For more detailed information on the development, principles, and applications of XPS, reference is made to the literature [37, 47, 48, 52].

References

1. V. Stadler, T. Felgenhauer, M. Beyer, S. Fernandez, K. Leibe, S. Güttler, M. Gröning, K. König, G. Torralba, M. Hausmann, V. Lindenstruth, A. Nesterov, I. Block, R. Pipkorn, A. Poustka, F.R. Bischoff, F. Breitling, Angew. Chem. Int. Ed. **47**, 7132–7135 (2008)
2. M. Beyer, I. Block, K. König, A. Nesterov, S. Fernandez, T. Felgenhauer, C. Schirwitz, K. Leibe, R. F. Bischoff, F. Breitling, V. Stadler, *Methods in Molecular Biology,* vol. 570. (Clifton, New Jersey, 2009), pp. 309–316
3. K. König, I. Block, A. Nesterov, G. Torralba, S. Fernandez, T. Felgenhauer, K. Leibe, C. Schirwitz, F. Löffler, F. Painke, J. Wagner, U. Trunk, F.R. Bischoff, F. Breitling, V. Stadler, M. Hausmann, V. Lindenstruth, Sens. Actuators, B: Chem. **147**, 418–427 (2010)
4. W. Kern, J. Electrochem. Soc. **137**, 1887–1892 (1990)
5. M. Beyer, T. Felgenhauer, F.R. Bischoff, F. Breitling, V. Stadler, Biomaterials **27**, 3505–3514 (2006)
6. O. Senftleben, H. Baumgärtner, I. Eisele, Mater. Sci. Forum. 573–574, 77–117 (2008)
7. V. Stadler, M. Beyer, K. König, A. Nesterov, G. Torralba, V. Lindenstruth, M. Hausmann, F.R. Bischoff, F. Breitling, J. Proteome Res. **6**, 3197–3202 (2007)
8. M. Grundner, H. Jacob, Appl. Phys. Solid Surf. **39**, 73–82 (1986)
9. A. Ulman, Chem. Rev. **96**, 1533–1554 (1996)
10. D.K. Schwartz, Annu. Rev. Phys. Chem. **52**, 107–137 (2001)
11. X. Huang, M.J. Wirth, Anal. Chem. **69**, 4577–4580 (1997)
12. J. Pyun, T. Kowalewski, K. Matyjaszewski, Macromol. Rapid Commun. **24**, 1043–1059 (2003)
13. A. Olivier, F. Meyer, J. M. Raquez, P. Damman, P. Dubois, *Progress in Polymer Science*, vol. 37. (Oxford press, Oxford, 2012), pp. 157–181
14. M. Kamigaito, T. Ando, M. Sawamoto, Chem. Rev. **101**, 3689–3745 (2001)
15. M. Kamigaito, Polym. J. **43**, 105–120 (2011)
16. M. Ouchi, T. Terashima, M. Sawamoto, Chem. Rev. **109**, 4963–5050 (2009)
17. J.S. Wang, K. Matyjaszewski, J. Am. Chem. Soc. **117**, 5614–5615 (1995)
18. V. Stadler, R. Kirmse, M. Beyer, F. Breitling, T. Ludwig, F.R. Bischoff, Langmuir **24**, 8151–8157 (2008)
19. F. Guillier, D. Orain, M. Bradley, Chem. Rev. **100**, 2091–2157 (2000)
20. N. Jung, M. Wiehn, S. Bräse, vol. 278, ed. by S. Brase, V. Balzani, A. Meijere, K. N. Houk, J. M. Lehn, H. Kessler, S. V. Ley, S. L. Schreiber, Top. Curr. Chem. **278**, 1–88 (2007)
21. R.B. Merrifield, J. Am. Chem. Soc. **85**, 2149–2154 (1963)
22. S.S. Wang, J. Am. Chem. Soc. **95**, 1328–1333 (1973)
23. M. Mergler, R. Tanner, J. Gosteli, P. Grogg, Tetrahedron Lett. **29**, 4005–4008 (1988)
24. M. Mergler, R. Nyfeler, R. Tanner, J. Gosteli, P. Grogg, Tetrahedron Lett. **29**, 4009–4012 (1988)
25. F. Albericio, G. Barany, Int. J. Pept. Protein Res. **30**, 206–216 (1987)

26. F. Albericio, N. Kneib-Cordonier, S. Biancalana, L. Gera, R.I. Masada, D. Hudson, G. Barany, J. Org. Chem. **55**, 3730–3743 (1990)
27. H. Rink, Tetrahedron Lett. **28**, 3787–3790 (1987)
28. S. Hoffmann, R. Frank, Tetrahedron Lett. **35**, 7763–7766 (1994)
29. G. Panke, R. Frank, Tetrahedron Lett. **39**, 17–18 (1998)
30. Y. Wolman, P.M. Gallop, A. Patchornik, J. Am. Chem. Soc. **83**, 1263–1264 (1961)
31. C. Peters, H. Waldmann, J. Org. Chem. **68**, 6053–6055 (2003)
32. J. Eichler, M. Bienert, A. Stierandova, M. Lebl, Pept. Res. **4**, 296–307 (1991)
33. M. Beyer, *Entwicklung und Anwendung neuartiger Trägeroberflächen zur kombinatorischen Peptidsynthese mit Aminosäure-Tonerpartikeln*, Ph.D. thesis, (University of Heidelberg, 2005)
34. G.B. Fields, R.L. Noble, Int. J. Pept. Protein Res. **35**, 161–214 (1990)
35. M. Gude, J. Ryf, P.D. White, Lett. Pept. Sci. **9**, 203–206 (2002)
36. I. Block, *Herstellung und Anwendung von hochkomplexen Peptidbibliotheken*, Ph.D. thesis, (University of Heidelberg, 2009)
37. C. R. Brundle, C. A. Evans, S. Wilson, *Encyclopedia of Materials Characterization: Surfaces, Interfaces, Thin Films* (Butterworth-Heinemann, Stoneham, 1992)
38. K. Vedam, Thin Solid Films 313–314, 1–9 (1998)
39. A.L. Cauchy, Bull. des Sci. Mathématiques **14**, 6–10 (1830)
40. H. Fujiwara, *Spectroscopic Ellipsometry: Principles and Applications* (Wiley, West Sussex, 2007)
41. R.F. Egerton, *Physical Principles of Electron Microscopy: An iItroduction to TEM, SEM, and AEM* 1st edn. (Springer, New York, 2005)
42. K. Shimizu, T. Mitani, *New Horizons of Applied Scanning Electron Microscopy*, vol. 45 (Springer, Heidelberg, 2009)
43. H. Hertz, Ann. Phys. **267**, 983–1000 (1887)
44. A. Einstein, Ann. Phys. **322**, 132–148 (1905)
45. C. Nordling, E. Sokolowski, K. Siegbahn, Phys. Rev. **105**, 1676–1677 (1957)
46. S. Hagström, C. Nordling, K. Siegbahn, Phys. Lett. **9**, 235–236 (1964)
47. M. Stamm, *Polymer Surfaces and Interfaces: Characterization, Modification and Applications*, 1st edn. (Springer, Berlin Heidelberg Germany, 2008)
48. T.L. Barr, *Modern ESCA: The Principles and Practice of X-ray Photoelectron Spectroscopy* (CRC Press, Boca Raton FL USA, 1994)
49. J.H. Scofield, J. Electron Spectrosc. Relat. Phenom. **8**, 129–137 (1976)
50. C.D. Bain, G.M. Whitesides, J. Phys. Chem. **93**, 1670–1673 (1989)
51. V. Stadler, *Chemische Nanolithographie mit Elektronenstrahlen an Biphenyl-Monoschichten*, Ph.D. thesis, (University of Heidelberg, 2001)
52. K. Siegbahn, *From X-Ray to Electron Spectroscopy*, vol. 746 (Springer, Berlin Heidelberg Germany, 2008)

http://www.springer.com/978-3-319-00806-6

Purification of Peptides in High-Complexity Arrays
A New Method for the Specific Surface Exchange and Purification of Entire Peptide Libraries

Schirwitz, C.

2013, XIII, 132 p. 59 illus., 53 illus. in color., Hardcover
ISBN: 978-3-319-00806-6